Check for updates

ChemCatChem

ChemCatChem
Chemistry Europe
European Chemical Societies Publishing

RESEARCH ARTICLE

Site-Blocking Poisoning of Pyridinic Nitrogen by Trace Formic Acid: Overcoming the Conversion Ceiling in Cumene Oxidation

Yuchan Deng[1] | Zhicheng Chen[2] | Yucheng Huang[1] | Guangxing Yang[2] | Qiao Zhang[2] | Yonghai Cao[1] | Feng Peng[2]

[1]School of Chemistry and Chemical Engineering, Guangdong Provincial Key Laboratory of Green Chemical Product Technology, South China University of Technology, Guangzhou, China | [2]School of Chemistry and Chemical Engineering, Guangzhou University, Guangzhou, China

Correspondence: Yonghai Cao (meyhcao@scut.edu.cn) | Feng Peng (fpeng@gzhu.edu.cn)

Received: 8 July 2026 | **Revised:** 12 October 2026 | **Accepted:** 10 November 2026

Keywords: carbon nanotubes | cumene oxidation | formic acid | liquid phase | N doping

ABSTRACT

Carbon-based nanomaterials frequently encounter a conversion bottleneck in the solvent-free aerobic oxidation of cumene. Using nitrogen-doped carbon nanotubes (NCNTs) and their manganese-modified composites as model catalysts, we observed the similar tendency of activity over these catalysts with the notable variation of the product distribution. Initial kinetic analyses showed that pyridinic N and metal sites accelerated the cleavage of primary hydroperoxides, lowering the apparent activation energy from 70.8 kJ/mol (for CNTs) to a range of 31.4–40.5 kJ/mol. However, the kinetic tracking and cross-validation experiments revealed that trace formic acid, generated from deep oxidation in the later reaction stages (~74.0% cumene conversion), caused severe catalyst deactivation. Density functional theory (DFT) calculations indicated that formic acid, a weak protic carboxylic acid, adsorbs strongly on pyridinic-N sites through acid–base interactions and hydrogen bonding, resulting in persistent site blocking. Herein, an interstage water-extraction strategy was employed to remove free formic acid from the organic reaction mixture. After interstage water extraction to remove dissolved formic acid and the addition of fresh NCNTs, the cumulative cumene conversion increased from 74.0% to 93.9%. By integrating mechanism elucidation with process intensification, this work establishes a theoretical and practical paradigm for overcoming conversion limits in liquid-phase oxidations.

1 | Introduction

The liquid-phase aerobic oxidation of hydrocarbons is an important process in industrial chemistry, transforming abundant petrochemical feedstocks into valuable oxygenated derivatives such as alcohols, ketones, and hydroperoxides. This transformation generally proceeds via a free-radical chain mechanism, which involves initiation, propagation, and termination stages [1–4]. The kinetic behavior of this process frequently depends on the decomposition of ROOH (ROOH→RO• + •OH) [5, 6], which replenishes radicals to sustain the chain reaction, yet this unimolecular decomposition is inherently slow under mild conditions [6–9]. While this fundamental mechanistic framework explains the autocatalytic nature of many oxidations, it also brings intrinsic kinetic limitations. As the reaction progresses, the intricate balance between radical generation and termination is often disrupted, leading to a deceleration and eventual stagnation of the reaction rate, a phenomenon known as the kinetic plateau. This plateau is widely observed in the oxidation of cumene (isopropylbenzene) to cumyl hydroperoxide (CHP), a key intermediate for phenol and acetone production [10]. Despite continuous optimization, achieving cumene conversion above

All rights reserved, including rights for text and data mining and training of artificial intelligence technologies or similar technologies.
© 2026 Wiley-VCH GmbH

90% remains a significant challenge, suggesting that intrinsic mechanistic constraints govern the final conversion.

This conversion limit is mainly caused by the self-regulating nature of the radical chain. First, the accumulation of oxygenated products, particularly alcohols like 2-phenyl-2-propanol, can inhibit the reaction. These alcohols act as radical scavengers, quenching propagating radicals and slowing down the chain reaction. For instance, in the carbon-catalyzed oxidation of ethylbenzene, adding 1-phenylethanol significantly suppressed the overall conversion rate [11]. Second, the intended product, CHP, plays a dual role. While its decomposition initiates new radical chains, high concentrations turn this decomposition into a side reaction, consuming the desired product without driving further substrate conversion. This causes a known trade-off between conversion and selectivity. For example, a Co–Ni bimetallic MOF catalyst exhibits ~91% selectivity to CHP but only achieves ~30% cumene conversion [12]. Similarly, a Pd/Ca–Al catalyst delivers 92.1% CHP selectivity with a conversion plateau at 52.0% [13]. Employing nitrogen-doped carbon nanotubes (NCNTs) can push the conversion to 72.1%, but the CHP selectivity drops significantly to 3.3%, favoring secondary products like acetophenone and CA [14]. Beyond these solution-phase limitations, the deactivation of the heterogeneous catalyst surface is another critical factor. During the later stages of oxidation, C-C bond cleavage inevitably generates trace amounts of low-carbon acidic byproducts, such as formic acid [11]. This raises a question: could these strongly adsorbing byproducts poison the catalyst's active sites, causing a deactivation that appears as a macroscopic kinetic plateau? Existing literature offers some hints. For instance, high loadings of NCNTs can inhibit the initial α-H abstraction step in ethylbenzene oxidation [15]. Also, transition metal oxides can inhibit cumene oxidation under certain conditions, particularly at high catalyst loadings. However, the direct link between the coverage of specific active sites (e.g., nitrogen functionalities) by such poisons and the observed conversion plateau remains unclear. This lack of understanding hinders the rational design of catalysts capable of breaking this conversion barrier.

To separate the effects of solution-phase inhibition and heterogeneous site deactivation, carbon-based materials, specifically nitrogen-doped carbons, serve as suitable model catalysts. Their well-defined surface chemistry, high structural stability, and ability to lower the activation energy for peroxide decomposition make them excellent models for studying the interface between solid surfaces and liquid-phase radical kinetics [6, 9, 16, 17]. In this work, we use nitrogen-doped carbon materials as model systems to investigate the origin of the conversion ceiling in cumene oxidation. Unlike previous studies focusing on general product inhibition, we establish a direct mechanistic link among the formation of trace formic acid during deep oxidation, its preferential occupation of pyridinic-N sites through acid–base interactions, the suppression of CHP decomposition, and the resulting conversion plateau. This mechanistic assignment is supported by kinetic tracking, product analysis, cross-validation experiments, and density functional theory calculations. Based on this, an interstage liquid-liquid extraction step, followed by the addition of fresh catalyst, was used to remove formic acid from the organic phase. This approach successfully increased the cumene conversion from 74.0% to 93.9%. These findings provide fundamental insights into how the reaction microenvironment drives catalyst deactivation, offering a practical strategy to sustain catalytic activity beyond the conventional ~90% conversion limit.

2 | Results and Discussion

To elucidate the regulatory mechanisms of the liquid-phase radical network and the origins of the late-stage conversion plateau, the initial catalytic performance of various model catalysts (pure CNTs, NCNTs, MnO/NCNTs, and MnO@NMC, Figures 1a–d and S3) was systematically evaluated under solvent-free conditions (Table 1). In the blank reaction without a catalyst, the cumene conversion was a mere 1.6%. Upon the introduction of pure CNTs, the conversion slightly increased to 11.4%, with a high selectivity of 91.4% toward the primary product, CHP. Microstructural observations via high-resolution transmission electron microscopy (HRTEM, Figure 1a) and Raman results revealed that pure CNTs possessed smooth walls with a low degree of defects (I_D/I_G = 0.7) (Figure S2). This indicates that while the unmodified carbon skeleton can adsorb substrates and initiate weak autoxidation, it lacks sufficient electron-donating capacity to cleave the high-activation-energy O—O bond. Consequently, the reaction experiences a deceleration shortly after the initial formation of CHP [18]. When the carbon skeleton was doped with nitrogen (NCNTs, Figures 1b and S4), the catalytic activity was substantially enhanced. The cumene conversion increased to 39.4%, accompanied by a significant shift in product distribution: the selectivity for CHP decreased, while the selectivities for the deep oxidation products acetophenone (AP) and 2-phenyl-2-propanol (PP) increased by approximately 5.8- and 8.7-fold, respectively. Compared to other reported catalysts, NCNTs exhibited a superior specific activity of 1704.8 mmol/g/h, outperforming traditional systems such as NHPI/$Co(acac)_2$ (5.1 mmol/g/h) and CuO (25.3 mmol/g/h) (Table S1) [19, 20]. To identify the microstructural origins of this enhanced activity, further characterization was performed. HRTEM showed that nitrogen doping induced localized wrinkling and increased defect density on the nanotube surface, correlating with a higher I_D/I_G ratio of 0.8. Furthermore, high-resolution N 1s XPS spectra indicated that pyridinic nitrogen dominated the NCNT surface (Figure S5, Tables S2, and S3). With its localized lone-pair electrons, pyridinic nitrogen exhibits strong Lewis basicity. Consistent with this view, Guo et al. demonstrated using well-defined HOPG model catalysts that pyridinic N creates Lewis-basic carbon sites adjacent to the nitrogen atoms, which facilitate O_2 adsorption and reduction [21]. This electron-donating property facilitates the cleavage of the O—O bond in CHP, thereby accelerating the generation of alkoxy radicals (RO•) and promoting chain propagation [22, 23].

The introduction of transition metals onto the nitrogen-doped carbon support (MnO/NCNTs and MnO@NMC, Figure 1c–d) further amplified the peroxide decomposition capacity [6, 24], making AP and PP the predominant products, while the overall cumene conversion correspondingly rose to 40.6%–44.3% (Table 1, entry 4–6). Microstructural analyses confirmed a synergistic effect between the metal and the support. HRTEM and HAADF–STEM images revealed highly dispersed MnO nanoparticles (Figures S6 and S7), approximately 2–4 nm in size, either supported on the carbon basal plane or encapsulated within mesoporous structures. XRD and XPS analyses corroborated the

18673899, 2026, 22, Downloaded from https://chemistry-europe.onlinelibrary.wiley.com/doi/10.1002/cctc.71177 by Yonghai Cao - South China University Of Technology , Wiley Online Library on [24/11/2026]. See the Terms and Conditions (https://onlinelibrary.wiley.com/terms-and-conditions) on Wiley Online Library for rules of use; OA articles are governed by the applicable Creative Commons License

TABLE 1 | The catalytic performance of cumene oxidation catalyzed by different catalysts[a].

Entry	Catalysts	S_{BET}[b] (m^2/g)	I_D/I_G[c]	R_s[d] (mmol/m^2/h)	R_m[e] (mmol/g/h)	Carbon blance (%)	X[f] (%)	Selectivity (%)		
										
1	Blank	—	—	—	—	100	1.3	—	—	100
2	CNTs	166.6	0.7	0.9	149.9	96.0	11.4	2	6.6	91.4
3	NCNTs	152.3	0.8	11.1	1704.8	89.3	39.4	10.0	39.7	50.3
4	MnO/NCNTs	153.6	0.8	10.0	1717.7	89.7	40.6	10.0	44.9	45.1
5	MnO@NMC	403.5	0.8	3.8	1540.9	88.8	44.3	8.7	40.7	50.5
6	MnO	1.55	—	68.1	105.5	97.3	11.7	12.3	54.8	32.8

[a]Reaction conditions: 20 mg catalyst, 10 mL cumene, 80°C, 25 mL/min O_2, 4 h.
[b]Specific surface areas (Figure S1).
[c]Raman spectra results (Figure S2).
[d]Initial rate of cumene consumption per m2 of catalyst surface.
[e]Initial rate of cumene consumption per gram of catalyst.
[f]The conversion of cumene.

18673899, 2026, 22, Downloaded from https://chemistry-europe.onlinelibrary.wiley.com/doi/10.1002/cctc.71177 by Yonghai Cao - South China University Of Technology , Wiley Online Library on [24/11/2026]. See the Terms and Conditions (https://onlinelibrary.wiley.com/terms-and-conditions) on Wiley Online Library for rules of use; OA articles are governed by the applicable Creative Commons License

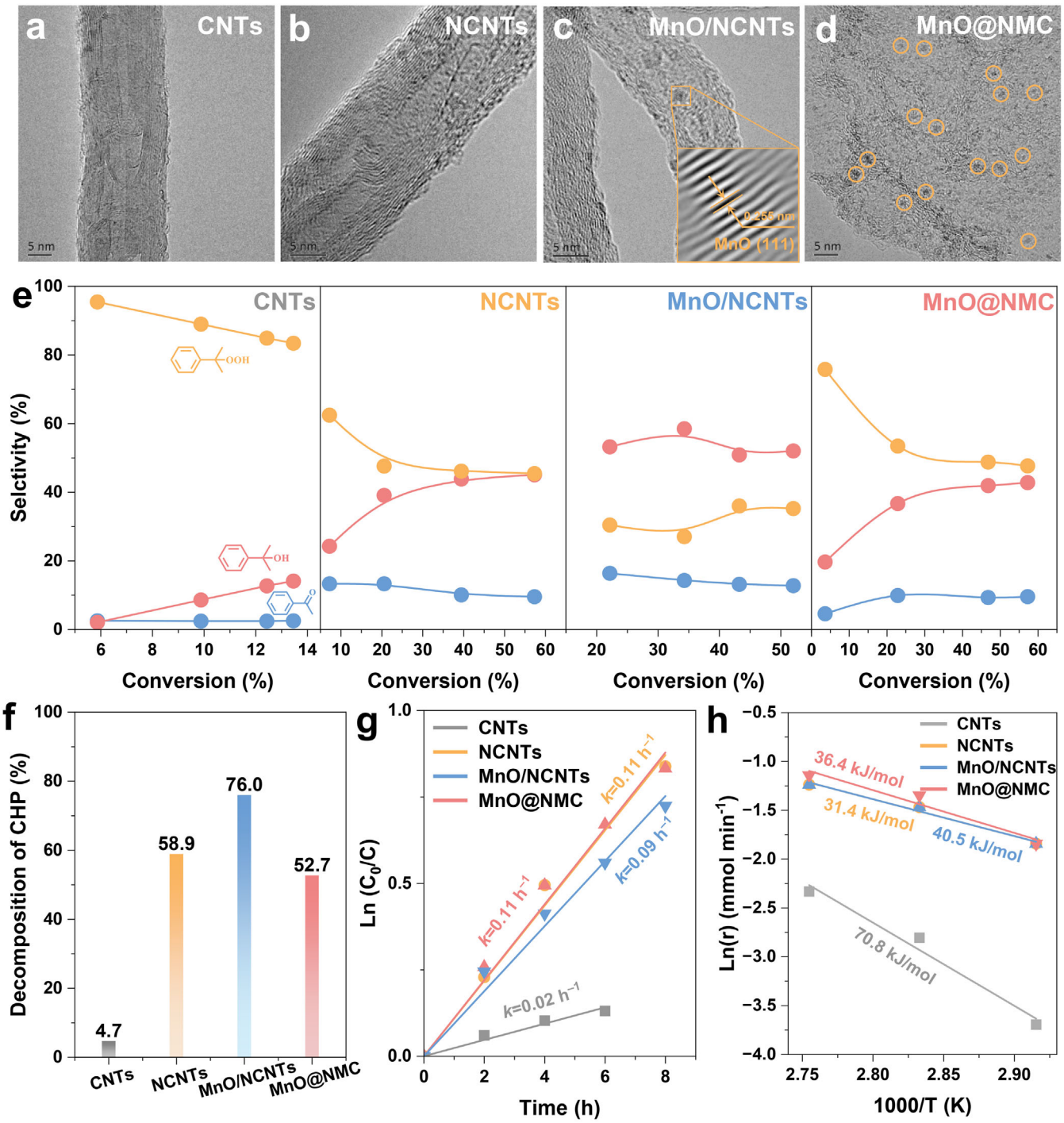

FIGURE 1 | The HRTEM images of model catalysts: (a) CNTs, (b) NCNTs, (c) MnO/NCNTs catalyst with inset showing FFT pattern of the (111) plane of MnO, and (d) MnO@NMC catalyst. (e) The cumene conversion versus the selectivities of products over different catalysts. (f) The decomposition of CHP over different catalysts. (g) Pseudo-first-order reaction fitting and (h) Arrhenius plots of cumene oxidation catalyzed by different catalysts.

presence of Mn^{2+} species (Figures S8–S10) [24]. Specifically, because the Mn *2p* spectra are highly susceptible to superficial oxidation upon ambient air exposure, the multiplet splitting of the Mn *3s* core level was utilized as a more robust metric. The measured splitting values of 6.0 and 6.1 eV for MnO/NCNTs and MnO@NMC, respectively, unambiguously verified that Mn(II) remained the predominant active phase [25–29]. Within this architecture, an electronic interaction between the electron-rich N-doped carbon and the MnO interface stabilizes the Mn^{2+}/Mn^{3+} redox couple, improving its electron transfer efficiency during CHP decomposition [30]. The typical mesoporous structure (pore size ~4.6 nm) and the high specific surface area (403.5 m^2/g) of the encapsulated MnO@NMC catalyst mitigated mass transfer limitations for bulky molecular species within the reaction network. Additionally, although pure bulk MnO achieved a similar macroscopic conversion (11.7%, Figure S11a), its massive agglomeration heavily restricted the exposure of active sites, resulting in a low mass-specific reaction rate (R_m) of 105.5 mmol/g/h.

18673899, 2026, 22, Downloaded from https://chemistry-europe.onlinelibrary.wiley.com/doi/10.1002/cctc.71177 by Yonghai Cao - South China University Of Technology , Wiley Online Library on [24/11/2026]. See the Terms and Conditions (https://onlinelibrary.wiley.com/terms-and-conditions) on Wiley Online Library for rules of use; OA articles are governed by the applicable Creative Commons License

Moreover, the XRD patterns of pure MnO after the reaction retained the characteristic reflections of cubic MnO, and no distinct diffraction peaks attributable to higher-valence crystalline MnO_x phases such as Mn_3O_4, Mn_2O_3, or MnO_2 were detected (Figure S11b). These results indicate that no detectable bulk crystalline phase transformation occurred under the present reaction conditions.

The dependence of product selectivity on conversion was evaluated over different catalysts (Figure 1e). For the pristine CNTs, CHP served as the primary product, maintaining a high selectivity of over 80% at low conversion levels (<15%). The introduction of NCNTs significantly shifted the product distribution toward deep oxidation. Compared to CNTs at similar conversion stages, the selectivity for CHP over NCNTs exhibited a pronounced decline to approximately 46%, accompanied by a concurrent increase in the selectivities for PP and AP. The integration of manganese species (MnO@NMC and MnO/NCNTs) further modulated the catalytic behavior. Across the evaluated conversion range, the deep oxidation pathways were enhanced over these composite catalysts, rendering PP and AP the predominant products, while the contribution of CHP was systematically suppressed. To decipher the origin of this selective shift, the decomposition capacities of the crucial intermediate, CHP, over different catalysts were quantified (Figure 1f). The CHP decomposition fraction over pure CNTs was constrained to merely 4.7%, indicating that while the carbon skeleton provides sufficient adsorption sites to initiate weak autoxidation, it lacks the electron-donating capability required to cleave the robust O—O bond. In contrast, NCNTs elevated this decomposition rate to 58.9%. This increase is attributed to the strong Lewis basicity rendered by the localized lone-pair electrons of pyridinic nitrogen, which effectively donates electron density to the peroxide bond. Furthermore, the metallic hybridization (MnO/NCNTs) peaked the decomposition fraction at 75.9%. The intensive electronic coupling between the N-doped carbon and the MnO interface acts to stabilize the dynamic Mn^{2+}/Mn^{3+} redox couple, thereby vastly refining the interfacial electron transfer efficiency during continuous CHP cleavage. Moreover, to quantify the kinetic effects of the different modification strategies during the reaction, the intense agitation was carried out across the whole reaction to exclude mass transfer limitations. Furthermore, the time-dependent cumene conversion and product selectivity profiles over the different catalysts are provided in Figure S12. As shown, unmodified CNTs maintained a high selectivity for CHP (>80%), but the conversion remained very low. In contrast, for the modified catalysts (NCNTs, MnO/NCNTs, and MnO@NMC), the conversion increased rapidly over time, while the selectivity for CHP decreased significantly. At the same time, the selectivities for the secondary products, PP and AP, steadily increased. These trends clearly show that the active nitrogen and metal sites effectively promote the further decomposition of the intermediate CHP. The pseudo-first-order reaction kinetics were fitted (Figure 1g), showing that the apparent reaction rate constants (k) for the modified catalysts (NCNTs, MnO/NCNTs, MnO@NMC) ranged from 0.09 to 0.11 h^{-1}, all of which were higher than that of pure CNTs (0.02 h^{-1}). Based on the Arrhenius plots (Figure 1h), heteroatom doping and metal modification effectively lowered the apparent activation energy (E_a) of the reaction from 70.8 kJ/mol (for pure CNTs) to a range of 31.4–40.5 kJ/mol.

Overall, the unifying feature of these modified carbon materials, whether through the construction of non-metallic Lewis basic sites or the incorporation of metallic redox couples, lies in their ability to accelerate CHP decomposition, thereby driving radical chain proliferation [31]. To provide experimental evidence for the radical pathway, the reaction mixture obtained after 4 h of cumene oxidation over NCNTs was analyzed by DMPO spin-trapping EPR spectroscopy. A characteristic multiline signal consistent with a DMPO–ROO• spin adduct was observed (Figure S13), supporting the involvement of peroxyl radicals in the cumene oxidation network [32]. However, this highly active deep oxidation process introduces a potential vulnerability. Despite structural differences, the similar initial kinetic parameters (k and E_a) among the N-doped and Mn-modified strategies suggest a shared underlying radical evolution pathway [33]. As conversion escalates, the extensive cleavage of peroxyl radicals intrinsically generates trace amounts of highly polar, low-carbon acidic byproducts in the later stages of the reaction. The relatively acidic and highly polar nature of these byproducts favors their competitive adsorption on basic or metal-containing surface sites [34, 35]. In particular, formic acid can interact preferentially with pyridinic-N sites through acid–base interactions and hydrogen bonding. This hypothesis provides a critical mechanistic clue for exploring the conversion plateau encountered by this catalytic system at later reaction stages.

To further investigate the long-term reaction performance of cumene oxidation, the relatively superior NCNTs and the unmodified CNTs were selected for extended kinetic tracking. As shown in Figure 2a, the cumene conversion over the pure CNT system did not exhibit significant improvement over time. In contrast, the conversion over the NCNT system initially increased almost linearly; however, after 12 h, the conversion curve distinctly leveled off, stagnating at approximately 74.0%. The conversion data at 12 and 16 h nearly overlapped, indicating that the reaction system faced a state of kinetic stagnation. Moreover, detailed time-dependent conversion, product selectivity, and estimated carbon-balance data are summarized in Table S4. The estimated carbon balance, calculated from the residual cumene and the quantified major liquid-phase products (AP, PP, and CHP), gradually decreased as the reaction proceeded, particularly over NCNTs. This trend suggests the progressive formation of additional carbon-containing products that were not included in the calculation during deep oxidation.

A comprehensive analysis of the liquid-phase mixture after 12 h of reaction was conducted to determine the cause of this conversion ceiling. Both gas chromatography (Figure 2b) and ion chromatography (Figure 2c) not only detected the conventional main products but also clearly identified the formation of a trace byproduct, formic acid. The major radical-chain pathways, including CHP formation and cleavage, PP and AP generation, and the deep-oxidation route yielding formic acid, are detailed as stoichiometrically balanced reactions in Equations S7–S21 [36]. Furthermore, the inhibitory effects of different products on the catalytic activity were evaluated. Experiments involving the addition of equivalent amounts of individual products to the initial reaction mixture (Figure 2d) revealed that conventional products (such as AP, PP, and CHP) did not impede the reaction, with the conversion maintaining at around 63%. Conversely,

18673899, 2026, 22, Downloaded from https://chemistry-europe.onlinelibrary.wiley.com/doi/10.1002/cctc.71177 by Yonghai Cao - South China University Of Technology , Wiley Online Library on [24/11/2026]. See the Terms and Conditions (https://onlinelibrary.wiley.com/terms-and-conditions) on Wiley Online Library for rules of use; OA articles are governed by the applicable Creative Commons License

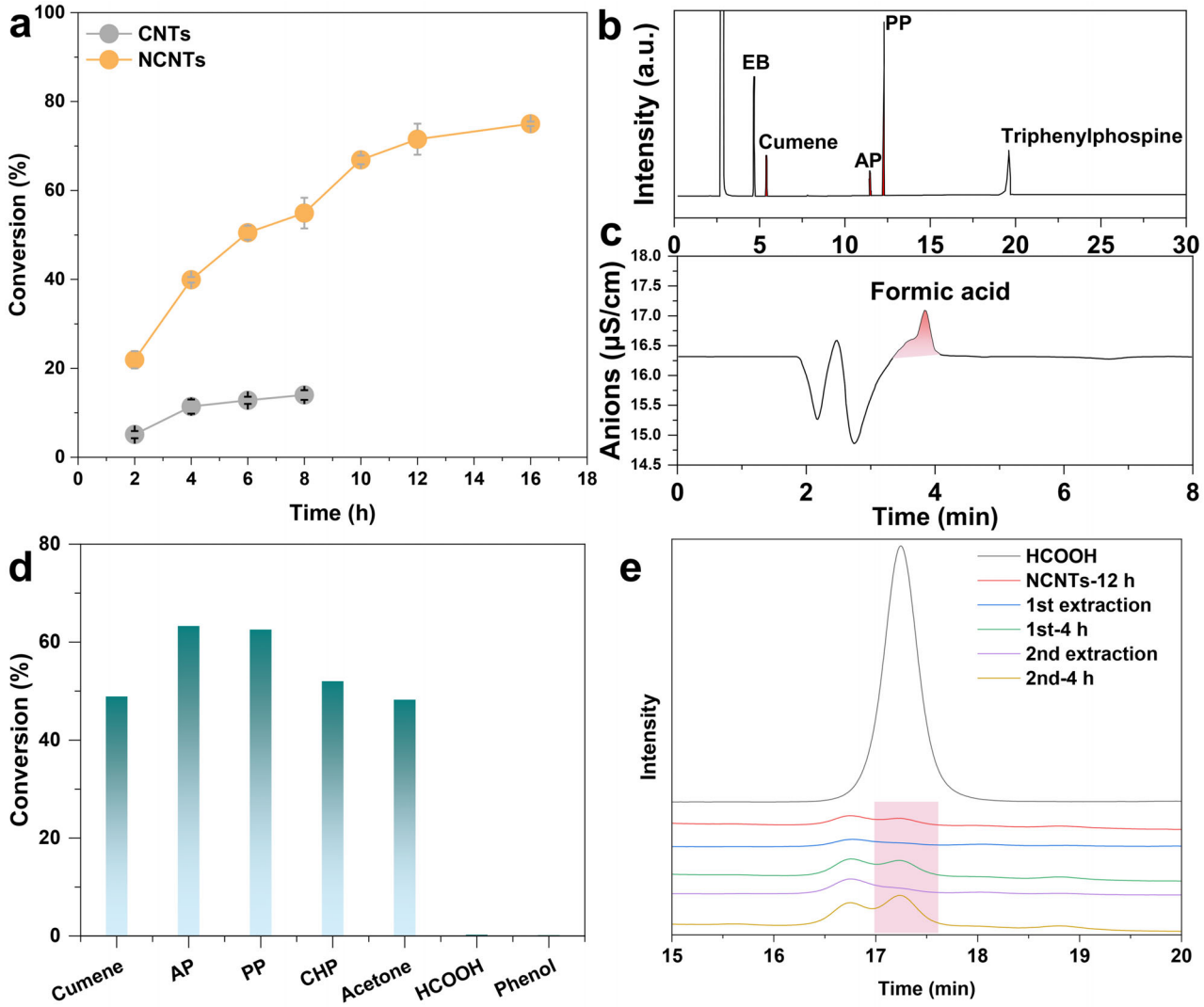

FIGURE 2 | (a) The conversion vs. time profiles for CNTs and NCNTs. (b) Gas chromatogram of the reaction solution for NCNTs-12 h; the identified peaks are assigned to acetophenone (AP), cumene, 2-phenyl-2-propanol (PP), and ethylbenzene (EB, internal standard). Before GC analysis, CHP was reduced to PP using triphenylphosphine. (c) Ion chromatogram of the reaction mixture for NCNTs-12 h. (d) The effect of different reaction products added to cumene on the activity. (e) The liquid chromatograms of the reaction solution before and after deionized water extraction.

the addition of formic acid severely suppressed the conversion to a negligible level. This result provided preliminary evidence that formic acid serves as the key inhibitor causing system deactivation.

To further elucidate the inhibition mechanism of formic acid and to rule out the possibility of a thermodynamic equilibrium induced by high main-product concentrations, a series of cross-validation experiments were designed (Table 2). First, the deactivation behavior on the catalyst surface was examined: the NCNTs recovered after an 8 h reaction were filtered, dried without washing (entry 2), and then subjected to a secondary 4 h reaction with fresh substrate, resulting in a low conversion of 22.9%. Compared to the pristine catalyst (entry 1), the catalytic activity was still prohibited. Notably, even after deep-washing the deactivated catalyst with deionized water and anhydrous ethanol (entry 3), the secondary conversion only marginally recovered to 29.3%. This indicates that formic acid underwent strong chemisorption on the carbon catalyst surface, which conventional washing processes failed to remove [35]. Next, the influence of the liquid-phase microenvironment was investigated. When the used catalyst was thermally regenerated via high-temperature annealing (to completely remove surface formic acid) and reintroduced into the original used reaction mixture from an 8 h run (entry 4), the conversion remained stagnant at 73.2%. This suggests that free formic acid remaining in the liquid phase rapidly reoccupies and poisons the cleaned active sites [37]. Finally, a simulated reaction mixture without formic acid was prepared based on the actual product concentrations at 12 h, to which a fresh catalyst was added (Entry 5). In this purified system, the cumene conversion reached 87.0%. These comparative results confirm that the late-stage reaction stagnation is not limited by intrinsic reaction equilibrium, but is rather attributed to site-blocking poisoning caused by the continuous accumulation of trace formic acid in the system [37, 38].

To unravel the origins of this strong chemical anchoring of formic acid on N-doped carbon materials at the molecular level,

18673899, 2026, 22, Downloaded from https://chemistry-europe.onlinelibrary.wiley.com/doi/10.1002/cctc.71177 by Yonghai Cao - South China University Of Technology , Wiley Online Library on [24/11/2026]. See the Terms and Conditions (https://onlinelibrary.wiley.com/terms-and-conditions) on Wiley Online Library for rules of use; OA articles are governed by the applicable Creative Commons License

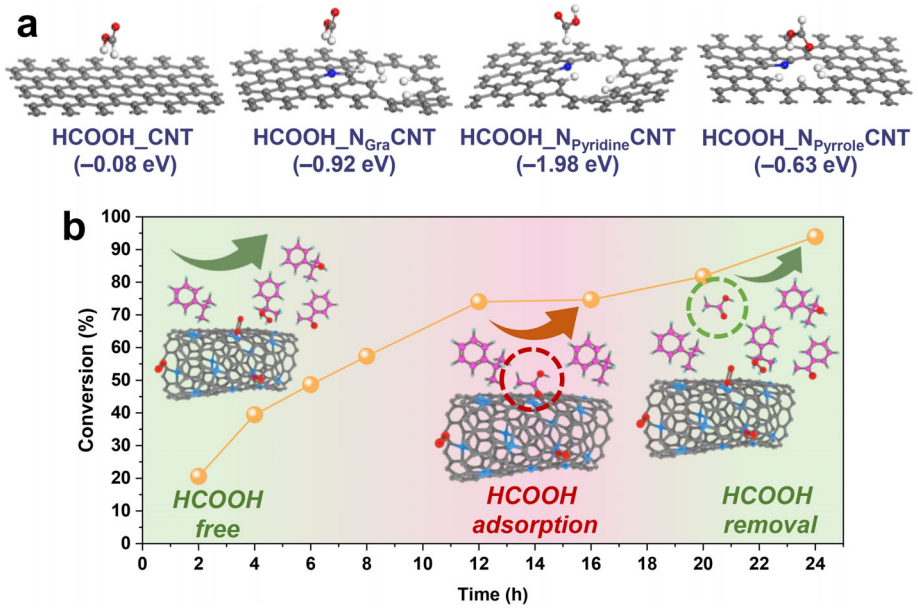

FIGURE 3 | (a) Formic acid adsorption configurations and energies on different nitrogen-doped carbon substrates. (b) The staged conversion profile of cumene oxidation coupled with interstage water extraction.

TABLE 2 | The cumene conversion underwent various treatment catalyzed by NCNTs.

Entry	Cumene conversion (%)		
	First run[a]	Second run[b]	Third run[b]
1	57.3	—	—
2	57.3	22.9[c]	—
3	57.3	29.3[d]	—
4	74.0	73.2[e]	—
5	—	87.0[f]	—
6	74.0[g]	81.8[h]	93.9[h]

[a]Conditions: 20 mg NCNTs, 10 mL cumene, 25 mL/min O_2, 8 h.
[b]Conditions: 20 mg NCNTs, 10 mL cumene, 25 mL/min O_2, 4 h.
[c]Used NCNTs without washing.
[d]Used NCNTs washed with ethanol.
[e]Pristine NCNTs added to the filtered reaction solution.
[f]Simulated solution with pristine NCNTs. A simulated reaction mixture representing the product composition at 12 h, but excluding formic acid, was prepared.
[g]12 h of reaction time.
[h]After each reaction stage, the spent catalyst was removed by filtration. The filtrate was extracted with 10 mL of deionized water in a separatory funnel by shaking for 5 min, followed by standing for 30 min for phase separation. The organic phase was collected and weighed, and fresh NCNTs were added proportionally to maintain the initial catalyst-to-liquid mass ratio. The reaction was then continued for another 4 h under an O_2 flow rate of 25 mL/min. The conversions of 81.8% and 93.9% are cumulative values calculated relative to the initial amount of cumene after the first and second extraction–reaction cycles, respectively.

DFT calculations were performed to evaluate the adsorption configurations and energies of formic acid on various carbon substrates (Figure 3a and Table S5). The calculations reveal that, compared to the extremely weak physisorption on pristine CNTs (−0.08 eV), the introduction of nitrogen atoms substantially enhances the material's affinity for formic acid [39]. Among the various nitrogen species, pyridinic N exhibits the strongest chemisorption energy (up to −1.98 eV) [40, 41], which aligns with the preceding experimental observations. As discussed in the initial performance analysis, pyridinic N serves as the core Lewis basic center that imparts excellent activity to NCNTs. However, its highly localized electron density makes it a preferential adsorption site for formic acid, a weak protic carboxylic acid [42]. The adsorption is mainly stabilized by acid–base interactions and hydrogen bonding, leading to the blockage of the catalytically active pyridinic-N sites. This fundamentally explains the microscopic mechanism behind the kinetic bottleneck encountered by this catalytic system in the later stages of the reaction [43].

Based on these mechanistic insights, a phase-separation intensification strategy was proposed at the reaction engineering level. For the stagnated reaction system (at 12 h, with a conversion of 74.0%, entry 6), a calculated volume of deionized water was introduced for liquid-liquid extraction. Leveraging the strong water solubility of formic acid, it was directionally separated from the hydrophobic organic reaction system. Liquid chromatography analysis (Figure 2e) confirmed that the residual formic acid signal in the organic phase was significantly attenuated after water extraction [44, 45]. Subsequently, when this purified reaction mixture was reacted further with fresh catalyst, the hindered chain reaction successfully resumed. The conversion increased to 81.8% after a single extraction, and after executing two consecutive extractions supplemented with fresh catalyst, the final cumene conversion broke through the previous limitation, reaching 93.9%. This process, coupling catalysis with separation, is summarized by the models in Figure 3b. In the initial reaction stage (HCOOH-free), the reaction network evolves freely, and the conversion rises steadily. As the reaction progresses, trace formic acid accumulates and anchors onto the pyridinic N sites (HCOOH adsorption), triggering catalyst poisoning and

18673899, 2026, 22, Downloaded from https://chemistry-europe.onlinelibrary.wiley.com/doi/10.1002/cctc.71177 by Yonghai Cao - South China University Of Technology , Wiley Online Library on [24/11/2026]. See the Terms and Conditions (https://onlinelibrary.wiley.com/terms-and-conditions) on Wiley Online Library for rules of use; OA articles are governed by the applicable Creative Commons License

reaction stagnation. The extraction step removed dissolved formic acid from the liquid phase, while the addition of fresh NCNTs supplied active sites for the subsequent reaction. This combination prevented the rapid poisoning of the newly introduced catalyst and allowed the reaction to resume. This study not only validates the micro-level product inhibition mechanism but also provides a practical engineering approach for breaking the conversion ceiling in industrial liquid-phase deep oxidation processes.

3 | Conclusion

Addressing the prevalent late-stage conversion stagnation in the solvent-free aerobic oxidation of cumene, this study elucidated the origin of catalyst deactivation and proposed an effective debottlenecking strategy by integrating microscopic molecular mechanism analysis with macroscopic process intensification. NCNTs and their Mn-modified composites leverage electron-rich pyridinic nitrogen and metal redox couples to accelerate the decomposition of CHP. This lowered the apparent activation energy from 70.8 kJ/mol (for CNTs) to 31.4–40.5 kJ/mol, yielding excellent initial reaction kinetics. However, cross-validation experiments and simulated reaction mixtures confirmed that the system-specific kinetic plateau of 74.0% observed over NCNTs under the present reaction conditions did not originate from thermodynamic equilibrium. Instead, it was caused by severe catalyst poisoning induced by trace formic acid, a deep oxidation byproduct generated in the later stages of the reaction. DFT calculations further indicated strong adsorption of formic acid, a weak protic carboxylic acid, on the highly active, basic pyridinic-N sites. The calculated adsorption energy reached −1.98 eV, far exceeding the physisorption energy on undoped carbon (−0.08 eV). This adsorption, mainly stabilized by acid–base interactions and hydrogen bonding, resulted in persistent site blocking that remained after conventional washing under the tested conditions. Based on this inhibition mechanism, an interstage water-extraction process was introduced. Utilizing aqueous phase separation, free formic acid molecules were efficiently extracted from the solution, thereby preventing continuous poisoning of the active sites. After dissolved formic acid was removed from the liquid phase and fresh NCNTs were added, the inhibited reaction resumed, and the cumulative cumene conversion reached 93.9%.

Author Contributions

Yuchan Deng: investigation, validation, writing – original draft, formal analysis. **Zhicheng Chen**: investigation, validation. **Yucheng Huang**: investigation, formal analysis. **Guangxing Yang**: writing – review and editing, formal analysis. **Qiao Zhang**: writing – review and editing. **Yonghai Cao**: conceptualization, writing – review and editing, funding acquisition, supervision. **Feng Peng**: conceptualization, supervision, writing – review and editing, funding acquisition.

Acknowledgments

We would like to acknowledge the financial support from the National Natural Science Foundation of China (21872041, 22272038), Guangdong Basic and Applied Basic Research Foundation (2026A1515010721), CNPC Innovation Found (2021DQ02-0704).

Conflicts of Interest

The authors declare no conflicts of interest.

Data Availability Statement

The data that support the findings of this study are available in the supporting information of this article

References

1. I. Hermans, P. A. Jacobs, and J. Peeters, "Understanding the Autoxidation of Hydrocarbons at the Molecular Level and Consequences for Catalysis," *Journal of Molecular Catalysis A: Chemical* (2006): 221–228, https://doi.org/10.1016/j.molcata.2006.02.005.

2. N. M. Emanuel, Z. K. Maizus, and I. P. Skibida, "The Catalytic Activity of Transition Metal Compounds in the Liquid-Phase Oxidation of Hydrocarbons," *Angewandte Chemie International Edition in English* 8 (2003): 97–107, https://doi.org/10.1002/anie.196900971.

3. S. Zoltowska, G. Chan, T. Tjardts, and P. Giusto, "One-Step Photocatalytic Oxidation of Cumene With Mesoporous Carbon Nitride," *ACS Catalysis* 16 (2026): 5654–5663, https://doi.org/10.1021/acscatal.5c08511.

4. Y. Ji, J. Zhao, H. Terazono, et al., "Reassessing the Atmospheric Oxidation Mechanism of Toluene," *Proceedings of the National Academy of Sciences* 114 (2017): 8169–8174, https://doi.org/10.1073/pnas.1705463114.

5. X. Yang, H. Wang, J. Li, et al., "Mechanistic Insight Into the Catalytic Oxidation of Cyclohexane over Carbon Nanotubes: Kinetic and In Situ Spectroscopic Evidence," *Chemistry–A European Journal* 19 (2013): 9818–9824, https://doi.org/10.1002/chem.201300676.

6. Y. Deng, Z. Chen, J. Huang, et al., "MnO_2 Nanoparticles Supported on CNTs for Cumene Oxidation: Synergistic Effect and Kinetic Modelling," *Chemical Engineering Journal* 444 (2022): 136666, https://doi.org/10.1016/j.cej.2022.136666.

7. L. Ding, X. Sun, C. Huang, J. Li, and B. Chen, "Insights Into the Mechanism of Cumene Catalytic Oxidation Using Ionic Liquid [Bmim]OH," *Molecular Catalysis* 538 (2023): 113008, https://doi.org/10.1016/j.mcat.2023.113008.

8. C. Mu, Y. Cao, H. Wang, H. Yu, and F. Peng, "A Kinetics Study on Cumene Oxidation Catalyzed by Carbon Nanotubes: Effect of N-doping," *Chemical Engineering Science* 177 (2018): 391–398, https://doi.org/10.1016/j.ces.2017.11.016.

9. E. Spier, U. Neuenschwander, and I. Hermans, "Insights Into the Cobalt(II)-Catalyzed Decomposition of Peroxide," *Angewandte Chemie International Edition* 52 (2013): 1581–1585, https://doi.org/10.1002/anie.201207920.

10. Y. Zhang, S. Wu, Y. Ma, et al., "Application, Characterization, and Simulation of CuO-ZnO-TiO_2 for Catalytic Oxidation of Cumene to Cumene Hydroperoxide," *Industrial & Engineering Chemistry Research* 64 (2025): 7670–7678, https://doi.org/10.1021/acs.iecr.4c04387.

11. A. Bhattacharya, "Kinetic Modeling of Liquid Phase Autoxidation of Cumene," *Chemical Engineering Journal* 137 (2008): 308–319, https://doi.org/10.1016/j.cej.2007.04.043.

12. A. Nowacka, P. Briantais, C. Prestipino, and F. X. Llabrés i Xamena, "Selective Aerobic Oxidation of Cumene to Cumene Hydroperoxide over Mono- and Bimetallic Trimesate Metal–Organic Frameworks Prepared by a Facile "Green" Aqueous Synthesis," *ACS Sustainable Chemistry & Engineering* 7 (2019): 7708–7715, https://doi.org/10.1021/acssuschemeng.8b06472.

13. S. Hao, J. He, Q. Tang, L. Liu, and J. Dong, "Constructing Highly Dispersed Pd on Ca-Al Layered Double Hydroxide for Efficiently Selective Oxidation of Cumene," *Molecular Catalysis* 568 (2024): 114490, https://doi.org/10.1016/j.mcat.2024.114490.

14. S. Liao, Y. Chi, H. Yu, H. Wang, and F. Peng, "Tuning the Selectivity in the Aerobic Oxidation of Cumene Catalyzed by Nitrogen-Doped Carbon

18673899, 2026, 22, Downloaded from https://chemistry-europe.onlinelibrary.wiley.com/doi/10.1002/cctc.71177 by Yonghai Cao - South China University Of Technology , Wiley Online Library on [24/11/2026]. See the Terms and Conditions (https://onlinelibrary.wiley.com/terms-and-conditions) on Wiley Online Library for rules of use; OA articles are governed by the applicable Creative Commons License

Nanotubes," *Chemcatchem* 6 (2014): 555–560, https://doi.org/10.1002/cctc.201300909.

15. W. Y. Suprun, R. B. Sheparovych, Y. M. Hrynda, O. Y. Khavunko, and I. A. Opeida, "Supported Transition Metals Oxides and N-hydroxyphthalimide as Binary Catalytic Systems for the Liquid-phase Oxidation of Cumene," *Molecular Catalysis* 510 (2021): 111683, https://doi.org/10.1016/j.mcat.2021.111683.

16. Z. Chen, Y. Deng, G. Yang, et al., "Understanding of Cumene Oxidation Catalyzed by Metal–Nitrogen–Carbon through Theoretical Simulations and Kinetic Validation," *ACS Sustainable Chemistry & Engineering* 11 (2023): 5773–5781, https://doi.org/10.1021/acssuschemeng.3c00676.

17. D. Duan, D. Chen, L. Huang, et al., "Activated Carbon From Lignocellulosic Biomass as Catalyst: A Review of the Applications in Fast Pyrolysis Process," *Journal of Analytical and Applied Pyrolysis* 158 (2021): 105246, https://doi.org/10.1016/j.jaap.2021.105246.

18. Y. Wu, J. Zhao, Q. Meng, M. Bi, C. Ma, and Z. Yu, "Effects of Oxygen: Experimental and VTST/DFT Studies on Cumene Autoxidation With Air under Atmospheric Pressure," *ACS Omega* 7 (2022): 34547–34553, https://doi.org/10.1021/acsomega.2c04362.

19. M. Zhang, L. Wang, H. Ji, B. Wu, and X. Zeng, "Cumene Liquid Oxidation to Cumene Hydroperoxide over CuO Nanoparticle With Molecular Oxygen under Mild Condition," *Journal of Natural Gas Chemistry* 16 (2007): 393–398, https://doi.org/10.1016/s1003-9953(08)60010-9.

20. K. Kasperczyk, B. Orlińska, and J. Zawadiak, "Aerobic Oxidation of Cumene Catalysed by 4-Alkyloxycarbonyl-N-Hydroxyphthalimide," *Open Chemistry* 12 (2014): 1176–1182, https://doi.org/10.2478/s11532-014-0565-8.

21. D. Guo, R. Shibuya, C. Akiba, S. Saji, T. Kondo, and J. Nakamura, "Active Sites of Nitrogen-Doped Carbon Materials for Oxygen Reduction Reaction Clarified Using Model Catalysts," *Science* 351 (2016): 361–365, https://doi.org/10.1126/science.aad0832.

22. A. T. N. Nguyen and J. H. Shim, "All Carbon Hybrid N-Doped Carbon Dots/Carbon Nanotube Structures as an Efficient Catalyst for the Oxygen Reduction Reaction," *RSC Advances* 11 (2021): 12520–12530, https://doi.org/10.1039/d1ra01197a.

23. K. Govindan, D.-G. Kim, and S.-O. Ko, "Role of N-Doping and O-Groups in Unzipped N-Doped CNT Carbocatalyst for Peroxomonosulfate Activation: Quantitative Structure–Activity Relationship," *Catalysts* 12 (2022): 845, https://doi.org/10.3390/catal12080845.

24. Z.-H. Diao, J.-C. Jin, M.-Y. Zou, et al., "Simultaneous Degradation of Amoxicillin and Norfloxacin by TiO_2@nZVI Composites Coupling with Persulfate: Synergistic Effect, Products and Mechanism," *Separation and Purification Technology* 278 (2021): 119620, https://doi.org/10.1016/j.seppur.2021.119620.

25. Y. Ding, J. Du, L. Guo, H. Zhou, H. Yang, and W. Feng, "Nanoscale MnO and Natural Graphite Hybrid Materials as High-Performance Anode for Lithium Ion Batteries," *Electrochimica Acta* 170 (2015): 9–15, https://doi.org/10.1016/j.electacta.2015.04.126.

26. Y. Xia, Z. Xiao, X. Dou, et al., "Green and Facile Fabrication of Hollow Porous MnO/C Microspheres From Microalgaes for Lithium-Ion Batteries," *ACS Nano* 7 (2013): 7083–7092, https://doi.org/10.1021/nn4023894.

27. W. Luo, X. Hu, Y. Sun, and Y. Huang, "Controlled Synthesis of Mesoporous MnO/C Networks by Microwave Irradiation and Their Enhanced Lithium-Storage Properties," *ACS Applied Materials & Interfaces* 5 (2013): 1997–2003, https://doi.org/10.1021/am302813d.

28. Y. Sun, X. Hu, W. Luo, F. Xia, and Y. Huang, "Reconstruction of Conformal Nanoscale MnO on Graphene as a High-Capacity and Long-Life Anode Material for Lithium Ion Batteries," *Advanced Functional Materials* 23 (2012): 2436–2444, https://doi.org/10.1002/adfm.201202623.

29. E. S. Ilton, J. E. Post, P. J. Heaney, F. T. Ling, and S. N. Kerisit, "XPS Determination of Mn Oxidation States in Mn (hydr)Oxides," *Applied Surface Science* 366 (2016): 475–485, https://doi.org/10.1016/j.apsusc.2015.12.159.

30. Z. Xie, Z. Lyu, J. Wang, A. Li, and F.-X. Corvini, "Ultrafine-Mn_2O_3@N-Doped Porous Carbon Hybrids Derived From Mn-MOFs: Dual-Reaction Centre Catalyst with Singlet Oxygen-Dominant Oxidation Process," *Chemical Engineering Journal* 429 (2022): 132299, https://doi.org/10.1016/j.cej.2021.132299.

31. J. Drönner, P. Hausoul, R. Palkovits, and M. Eisenacher, "Solid Acid Catalysts for the Hock Cleavage of Hydroperoxides," *Catalysts* 12 (2022): 91, https://doi.org/10.3390/catal12010091.

32. Y. Wang, Y. Zhou, W. Sun, X. Wang, J. Yao, and H. Li, "Identifying Radical Pathways for Cu(I)/Cu(II) Relay Catalyzed Oxygenation via Online Coupled EPR/UV–Vis/Near-IR Monitoring," *Advanced Science* 11 (2024): e2402890, https://doi.org/10.1002/advs.202402890.

33. S. Vyazovkin, "A Time to Search: Finding the Meaning of Variable Activation Energy," *Physical Chemistry Chemical Physics* 18 (2016): 18643–18656, https://doi.org/10.1039/c6cp02491b.

34. T. Lu, G. Li, W. Wu, et al., "Alkali-Oxygen Oxidation Mechanism for Producing Benzene Carboxylic Acids From Lignite: Experimental and Molecular Modelling Studies," *Fuel* 280 (2020): 118652, https://doi.org/10.1016/j.fuel.2020.118652.

35. H. A. Abdullah, C. H. Rochester, J. A. Anderson, J. E. Bailie, N. V. Richardson, and G. J. Hutchings, "Effects of Carboxylic Acid Adsorbates on CO Adsorption and Crotonaldehyde Hydrogenation Over Cu/Al_2O_3 Catalyst," *Physical Chemistry Chemical Physics* 2 (2000): 3925–3932, https://doi.org/10.1039/b003429k.

36. A. Bhattacharya, "Kinetic Modeling of Liquid Phase Autoxidation of Cumene," *Chemical Engineering Journal* 137 (2008): 308–319, https://doi.org/10.1016/j.cej.2007.04.043.

37. G. Pipitone, A. J. R. Hensley, A. Omoniyi, G. Zoppi, R. Pirone, and S. Bensaid, "Unravelling Competitive Adsorption Phenomena in the Aqueous Phase Reforming of Carboxylic Acids on Pt Catalysts: An Experimental and Theoretical Study," *Chemical Engineering Journal* 482 (2024): 148902, https://doi.org/10.1016/j.cej.2024.148902.

38. I. M. S. Anekwe and Y. M. Isa, "Unlocking Catalytic Longevity: A Critical Review of Catalyst Deactivation Pathways and Regeneration Technologies," *Energy Advances* 4 (2025): 1075–1113, https://doi.org/10.1039/d5ya00015g.

39. F. Sun, J. Gao, X. Liu, Y. Yang, and S. Wu, "Controllable Nitrogen Introduction into Porous Carbon with Porosity Retaining for Investigating Nitrogen Doping Effect on SO_2 Adsorption," *Chemical Engineering Journal* 290 (2016): 116–124, https://doi.org/10.1016/j.cej.2015.12.044.

40. M. Wang, X. Fan, L. Zhang, et al., "Probing the Role of O-containing Groups in CO_2 Adsorption of N-doped Porous Activated Carbon," *Nanoscale* 9 (2017): 17593–17600, https://doi.org/10.1039/c7nr05977a.

41. K. A. Dmitruk, I. A. Podolyako, D. A. Shlyapin, A. A. Shubin, and O. V. Netskina, "Adsorption of CO_2 on N-Doped Carbon Materials: The Effect of the Subsurface Layer," *Surface Science* 762 (2025): 122819, https://doi.org/10.1016/j.susc.2025.122819.

42. R. Ma, B. Y. Xia, Y. Zhou, et al., "Ionic Liquid-Assisted Synthesis of Dual-Doped Graphene as Efficient Electrocatalysts for Oxygen Reduction," *Carbon* 102 (2016): 58–65, https://doi.org/10.1016/j.carbon.2016.02.034.

43. C. H. Bartholomew, "Mechanisms of Catalyst Deactivation," *Applied Catalysis A: General* 212 (2001): 17–60, https://doi.org/10.1016/s0926-860x(00)00843-7.

44. H. Veith, M. Voges, C. Held, and J. Albert, "Measuring and Predicting the Extraction Behavior of Biogenic Formic Acid in Biphasic Aqueous/Organic Reaction Mixtures," *ACS Omega* 2 (2017): 8982–8989, https://doi.org/10.1021/acsomega.7b01588.

45. S. Zou, Y. Zhao, P. Li, H. Chang, and Y. Li, "Liquid–Liquid Equilibria of Formic Acid and Furfural in a Biphasic Aqueous–Organic System: Optimization of Solvent and Amine Extractant," *Journal of Chemical &*

18673899, 2026, 22, Downloaded from https://chemistry-europe.onlinelibrary.wiley.com/doi/10.1002/cctc.71177 by Yonghai Cao - South China University Of Technology , Wiley Online Library on [24/11/2026]. See the Terms and Conditions (https://onlinelibrary.wiley.com/terms-and-conditions) on Wiley Online Library for rules of use; OA articles are governed by the applicable Creative Commons License

Engineering Data 63 (2018): 4314–4324, https://doi.org/10.1021/acs.jced.8b00335.

46. C.-O. L. Crites, G. L. Hallett-Tapley, M. Frenette, M. González-Béjar, J. C. Netto-Ferreira, and J. C. Scaiano, "Insights into the Mechanism of Cumene Peroxidation Using Supported Gold and Silver Nanoparticles," *ACS Catalysis* 3 (2013): 2062–2071, https://doi.org/10.1021/cs400337w.

47. J. Deng, Y. Li, Y. Cao, et al., "Trace Amounts of $Cu(OAc)_2$ Boost the Efficiency of Cumene Oxidation Catalyzed by Carbon Nanotubes Washed With HCl," *Catalysis Science & Technology* 10 (2020): 2523–2530, https://doi.org/10.1039/c9cy02536g.

48. S. Liao, F. Peng, H. Yu, and H. Wang, "Carbon Nanotubes as Catalyst for the Aerobic Oxidation of Cumene to Cumene Hydroperoxide," *Applied Catalysis A: General* 478 (2014): 1–8, https://doi.org/10.1016/j.apcata.2014.03.024.

49. Q. Lu, G. Shi, H. Zhou, E. Yuan, C. Chen, and L. Ji, "A Highly Efficient Transformation From Cumene to Cumyl Hydroperoxide via Catalytic Aerobic Oxidation at Room Temperature and Investigations Into Solvent Effects, Reaction Networks and Mechanisms," *Applied Catalysis A: General* 630 (2022): 118441, https://doi.org/10.1016/j.apcata.2021.118441.

50. S. Xu, J. Zhang, B. Chen, and Z. Lei, "Process Intensification on the Selective Catalytic Oxidation of Cumene with Ionic Liquids," *Chemical Engineering and Processing—Process Intensification* 130 (2018): 88–92, https://doi.org/10.1016/j.cep.2018.06.002.

51. M. Yang, G. Qiu, C. Huang, X. Han, Y. Li, and B. Chen, "Selective Oxidation of Cumene to the Equivalent Amount of Dimethylbenzyl Alcohol and Cumene Hydroperoxide," *Industrial & Engineering Chemistry Research* 58 (2019): 19785–19793, https://doi.org/10.1021/acs.iecr.9b03476.

Supporting Information

Additional supporting information can be found online in the Supporting Information section.

The chemical reagents, characterizations, and related discussions can be found in the Supporting Information. The authors have cited additional references within the Supporting Information [12, 13, 16, 19, 20, 46–51].

Supporting File 1: cctc71177-sup-0001-SuppMat.pdf

18673899, 2026, 22, Downloaded from https://chemistry-europe.onlinelibrary.wiley.com/doi/10.1002/cctc.71177 by Yonghai Cao - South China University Of Technology , Wiley Online Library on [24/11/2026]. See the Terms and Conditions (https://onlinelibrary.wiley.com/terms-and-conditions) on Wiley Online Library for rules of use; OA articles are governed by the applicable Creative Commons License